

Untethered soft microrobot driven by a single actuator for agile navigations

Received: 18 January 2025

Accepted: 30 June 2025

Published online: 25 July 2025

 Check for updatesYichuan Wu¹✉, Lai Cao¹, Guobin Lu¹, Peng Wang², Longqi Ran¹ & Bei Peng¹

Cockroaches are renowned for their ability to swiftly navigate through tight spaces and robustly withstand high impacts due to their well-controlled locomotion and highly flexible exoskeletons. It has been a long-standing challenge to replicate these features in untethered controllable microrobots (weighing ~1 g). Here, we show that a single actuator is used to tune a microrobot's leg strokes for controllable movements in various directions (forward, backward, and diagonal). Weighing just over 1 g and measuring 2 cm in length, the untethered microrobot achieves a forward speed of 4.8 body lengths per second (BL/s) and a turning speed of 280 deg/s, resulting in an outstanding maneuverability that has only previously been achieved in multiply-actuated microrobots. The untethered microrobot can remain functional after being stepped on. The single actuator driving scheme, device structural architecture, and control techniques are investigated as key guidance for the development of future controllable and resilient miniaturized robots.

Tiny robots (~1 g) with the inspiration of living insects hold significant potential for applications in confined working environments, such as search and rescue operations, infrastructure inspections, and medical interventions. However, the development of untethered and miniaturized robots presents significant challenges to achieve full autonomy of mobility^{1–8}. Most mobile microrobots capable of sustained operations rely on external power sources, such as direct physical connections through electrical wires^{9–18}, energy harvesting from environmental sources such as light/heat^{19–21}, humidity^{22,23}, or remotely supplied power via electromagnetic fields^{24–27}. Recent developments have showcased impressive battery-powered robotic systems using lightweight and compliant actuators but they still encounter limitations in operational capabilities, such as locomotion speed, steering agility, and structural robustness^{28–30}.

It is generally considered among robotics researchers that increasing the number of actuators will enhance maneuverability. Although in-plane maneuverability with a single actuator has been shown with the 80-gram IStar robot³¹, it is easy to add extra actuators at this size scale, for example using DC motors. However, as the scale of robots approaches the 1-gram mark, integrating multiple actuators becomes increasingly difficult, and can reduce robustness. Incorporating multiple actuators for tunable strokes to

control mobility often leads to undesirable increases in the weight, size, and operation complexity. This approach also tends to compromise a microrobot's resilience due to the fragility of multiple driving modules^{32,33}. On the other hand, biological entities such as cockroaches exhibit remarkable robustness, capable of withstanding extremely large forces and deformations without sustained injury, owing to their flexible exoskeletons³⁴. In this work, we use a single soft actuator to achieve tunable leg strokes in a microrobot to deliver fast and controllable locomotion while maintaining a high level of endurance and simplicity, which encompasses several key advancements: **(i)** using a single actuator to tune leg strokes for both upright and upside-down posture motions such as forward, backward, clockwise (CW) and counter-clockwise (CCW); **(ii)** a compact form factor of 1.12 grams in weight and 2 centimeters in length that achieves a high maneuverability of a forward running speed of 4.8 BL/s and an angular turning speed of 280 deg/s; **(iii)** highly compressible exoskeletons to withstand 53,000 times heavier loads stepped by an adult without compromising its moving speed; and **(iv)** untethered motion demonstrations including endurance of free-fall tests, closed-loop trajectory control, navigation through constricted tubes, and the ability to traverse on the water surface.

¹School of Mechanical and Electrical Engineering, University of Electronic Science and Technology of China, Chengdu 611731, China. ²Department of Mechanical Engineering, Tsinghua University, Beijing 100084, China. ✉e-mail: yichuanwu@uestc.edu.cn

Results

Design concept and working principle

Fig. 1a shows an optical image of a base structure of the microrobot, measuring 2 cm in length and 260 mg in weight, alongside a U.S. quarter coin. The base structure has a unimorph actuator at the top, front and rear exoskeletons for directional control, and a central carbon-fiber frame as a stabilization platform to carry payloads such as onboard batteries and circuits. Detailed material properties and fabrication methods are provided in Supplementary Table 1 and Fig. 1. The layered piezoelectric actuator is about 30 mg and serves as the single artificial muscle. The cross-sectional scanning electron microscopy (SEM) image (inset of Fig. 1a) reveals its composition: a 25- μm -thick polyethylene terephthalate (PET) top layer, a 25- μm -thick adhesive

silicone middle layer, and a 20- μm -thick Polyvinylidene difluoride (PVDF) bottom layer, sandwiched by two 55-nm-thick metal electrode layers (5 nm Cr and 50 nm Au). The actuator is connected to a carbon-fiber frame via the front and rear exoskeletons, each made from a 120- μm -thick polyimide (PI) film. These exoskeletons, designed with tuning fork-shaped legs and short serpentine, facilitate soft transmission and suspension mechanisms. The PET/PVDF unimorph actuator changes its curvature periodically under several hundreds of alternating current (AC) voltages by the piezoelectric effect⁹. This elastic actuator activates the robot's movements by alternately pushing and pulling the front and rear exoskeletons, enabling the legs to strike against the ground to facilitate locomotion. In the exoskeleton design, the stroke amplitude measured at the end of a leg is about twice that of the

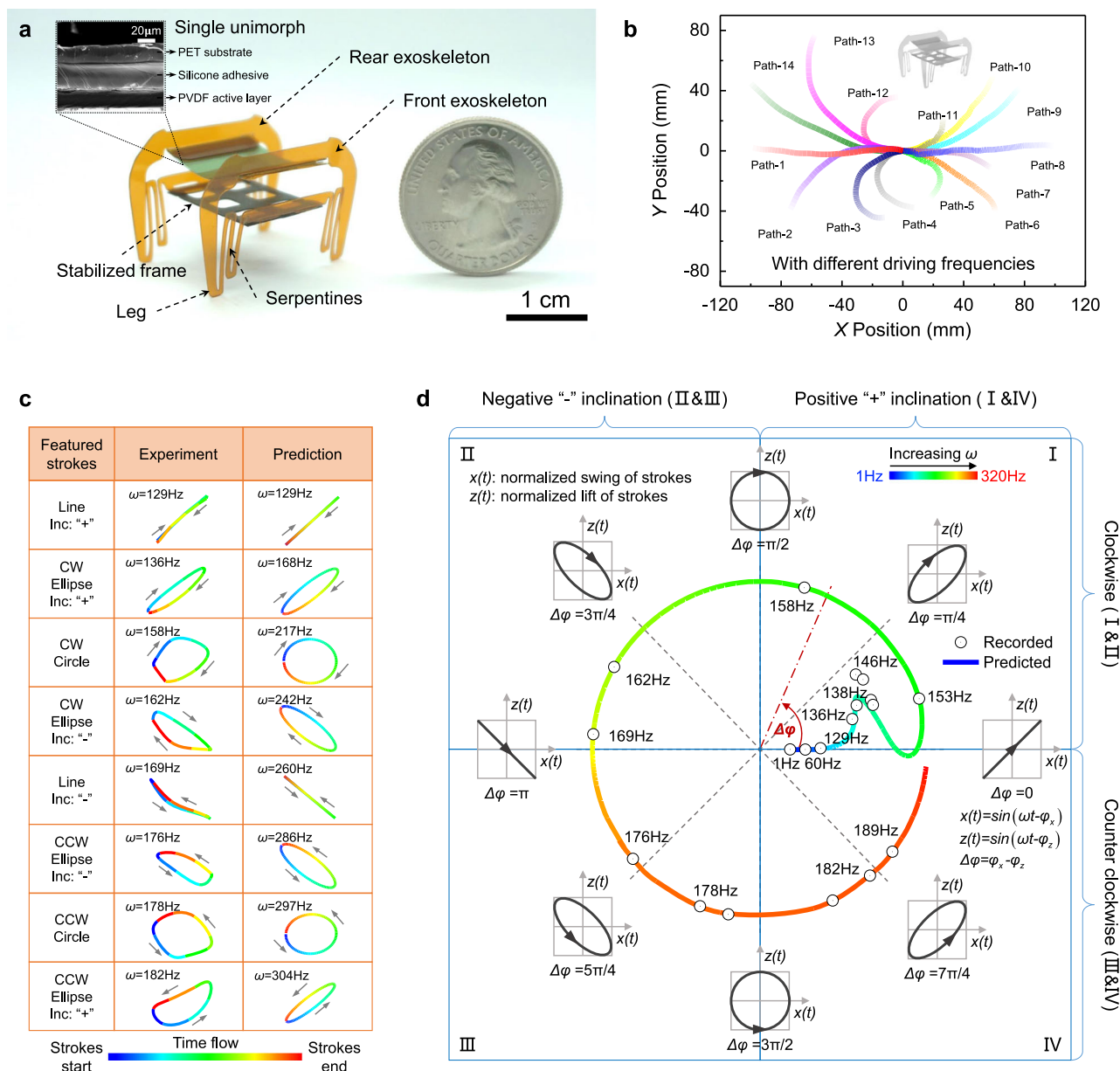


Fig. 1 | The prototype robot and its stroke-tuning ability with a single actuator. **a** Optical image of a base robot alongside a U.S. quarter. The main body consists of a unimorph, two exoskeletons, and a stabilized carbon-fiber frame. The inset SEM image shows a cross-sectional view of the unimorph. **b** With different driving frequencies, the single actuator robot demonstrates various experimental paths, including forward, backward, and diagonal directions. **c** Eight featured strokes are observed from an individual leg in experiments and predictions, respectively. **d** The

map of increasing driving frequency and its effects on phase shifts, as well as stroke shapes, orientations, and inclinations. The patterns of strokes are dominated by the phase shifts $\Delta\phi$ between the swing $x(t)$ and lift $z(t)$. The units of x and z directions are normalized. The continuous curve colors indicate the predicted strokes given the driven frequency while the discrete dots indicate the recorded experimental results. See Supplementary Movie 3. Frequencies increase from blue (low frequency) to red (high frequency).

actuator movements measured at the middle of the PVDF under the first resonant mode (Supplementary Fig. 2). Equipped with this single actuator, the prototype robot has demonstrated a variety of locomotion trajectories from Path-1 to Path-14 as shown in Fig. 1b with different driving frequencies. Detailed depictions of the robot's movements, including forward, right, back left, backward, back right, and left motions, are illustrated in Supplementary Fig. 3 and Movie 1. Interestingly, under the upside-down posture, the microrobot also has controlled movements for agile navigations as shown in Supplementary Fig. 4–5 and Movie 2. The directional steering control with a single actuator drastically compacts the robotic system in favor of enhanced maneuverability and obstacle avoidance. The turning strategy is advantageous compared to conventional methods that rely on two or more actuators and thus have increased weight and complexity of control mechanisms.

Analysis of leg strokes

The strokes' tuning mechanism based on a single actuator is analyzed theoretically with numerical simulations and experimental verifications. The robot's middle frame is first fixed on a stage and two high-speed cameras (4000 frames per second) are positioned at two sides of the robot to observe leg strokes (setup in Supplementary Fig. 6). As an example, a coordinate system is established along the strokes of the left front leg, where x represents longitudinal swing and z represents vertical lift (Supplementary Fig. 7). The lateral y motions are quite small and neglected because the piezoelectric actuator mainly induces x and z displacements in the d_{31} mode. Various leg stroke patterns can be excited and recorded with respect to the driving frequency of the single actuator (Supplementary Movie 3) and eight featured stroke patterns are identified in Fig. 1c: line-shape strokes with positive inclination, CW elliptical strokes with positive inclination, CW circular strokes, CW elliptical strokes with negative inclination, line-shaped strokes with negative inclination, CCW elliptical strokes with negative inclination, CCW circular strokes, and CCW elliptical strokes with positive inclination. These patterns are characterized by their shapes (lines, circles, or ellipses), striking orientations (CW or CCW), and angular inclinations (positive or negative) as the motion control schemes.

A precise mathematical model to describe the observed phenomena is not possible such that a linear approximation is used to explain the soft robot's dynamics with modal analysis. A physical model is built in Supplementary Fig. 8 and its mode shapes are simulated using COMSOL software. By treating the vibration mode k (k indicates the k -th natural frequency of the robot) independently, the total displacement in the x (longitudinal) and z (vertical) directions is approximated by summing the normal modes multiplied by their respective contribution weight q_k . The terms U_k and W_k denote the k -th normalized mode shapes in the x and z directions, respectively, and N indicates the number of modes considered.

$$\begin{bmatrix} x \\ z \end{bmatrix} = \begin{bmatrix} \sum_{k=1}^N U_k q_k \\ \sum_{k=1}^N W_k q_k \end{bmatrix} \quad (1)$$

The first 30 natural frequencies are listed in Supplementary Table 2, and the simulated mode shapes are shown in Supplementary Fig. 9 and Movie 4. These modes depend only on coordinates, while the time-dependent modal coordinate q_k characterizes oscillation in the k -th mode. Modal analysis captures the leg displacement in both x and z directions, allowing leg strokes to be delineated at any given driving frequency ω . Comparison of the featured strokes from experiment and prediction show good agreement (Fig. 1c). The details for qualitative introduction to strokes' tuning mechanisms with a single actuator are discussed in Supplementary Method 1. The linear

system analysis reveals that the dynamic response in each direction resonates with the imposed driving frequency. Hence, the normalized displacement in x and z directions can be described by

$$x = \sin(\omega t - \varphi_x) \quad (2)$$

$$z = \sin(\omega t - \varphi_z) \quad (3)$$

Phases φ_x and φ_z can exhibit variable offsets as the driving frequency ω changes. It can be found that relative phase shifts $\Delta\varphi = \varphi_x - \varphi_z$ dominate stroke shapes (lines, ellipses, or circles), orientations (CW or CCW), and inclinations (positive or negative). We focus on the influence of phase shifts on stroke patterns so that the amplitudes of x and z directions are normalized in Fig. 1d. The map of stroke patterns determined by phase shift is detailed in Supplementary Fig. 10. Fig. 1d shows the relationships between the driving frequency and its effects on phase shifts, as well as the corresponding stroke shapes, orientations, and inclinations. The continuous curves show the predicted stroke patterns and values of phase shifts given a range of the driving frequency (from blue to red). Specifically, a zero-phase difference ($\Delta\varphi = 0$) results in a linear stroke pattern with positive inclination to the horizontal axis (x). Conversely, a phase shift of π aligns the pattern linearly but with negative inclination. CW circles emerge when $\Delta\varphi = \pi/2$, and CCW circles when $\Delta\varphi = 3\pi/2$. Ellipses with various inclinations and orientations appear with other phase shift values. Fig. 1d highlights two critical findings: (1) orientation transitions (between CW and CCW) occur when $\Delta\varphi$ crosses 0 or π , and (2) inclination exchanges (between positive and negative) occur as $\Delta\varphi$ approaches $\pi/2$ or $3\pi/2$. The recorded phase shifts $\Delta\varphi$ (discrete dots) are approximated by the fundamental components of Fourier Transform (Supplementary Fig. 11 and 12) while the predicted phase shifts $\Delta\varphi$ (continuous curves) are achieved by modal analysis (Supplementary Method 1). The comparison of experimental and predicted strokes shows good alignment in trends as the driving frequency ω transitions from low to high (Fig. 1d and Supplementary Movie 3). Both the recorded and predicted strokes can be continuously regulated among the four quadrants (I, II, III, and IV) as the driving frequency changes. The discrepancies between the experimental results and the model predictions are speculated to be primarily attributed to assembly variations inherent in the manual fabrication process of the robot, as detailed in Supplementary Fig. 13–14 and Method 1.

A series of predicted strokes, approximated by summing 30, 45, and 50 vibration modes, are shown in Supplementary Fig. 15, covering a diverse range of shapes (lines, ellipses, and circles), orientations (CW and CCW), and inclinations (positive and negative). Supplementary Fig. 16 and 17 display predictions using 5 and 15 modes, respectively. For comparison, Supplementary Fig. 18 summarizes the predicted phase shifts and strokes with different modes approximation. For $N = 5$ modes (black curves), there are no phase shifts ($\Delta\varphi = 0$) between x and z directions as the driving frequency ω changes. As a result, the leg strokes appear only as lines with positive inclination, meaning they cannot be tuned by adjusting ω , and a robot would be unable to steer. For $N = 15$ modes (red curves), phase shifts $\Delta\varphi$ vary between 0 and $\pi/2$ as ω changes. This produces strokes with CW orientations or lines with positive inclinations but lacks CCW orientations or negative inclinations. Consequently, using the first 15 modes allows a robot's backward locomotion but prevents forward movement (left is defined as forward direction). For higher mode numbers, such as $N = 45$ (green curves) and $N = 50$ (purple curves), the resulting strokes closely resemble those obtained with $N = 30$ (blue curves). These strokes exhibit diverse shapes, orientations, and inclinations, aligning well with the trend observed in our experimental data (discrete dots in Fig. 1d). Thus, we conclude that selecting the first 30 mode shapes is sufficient for the robot's steering mechanism. A diverse range of

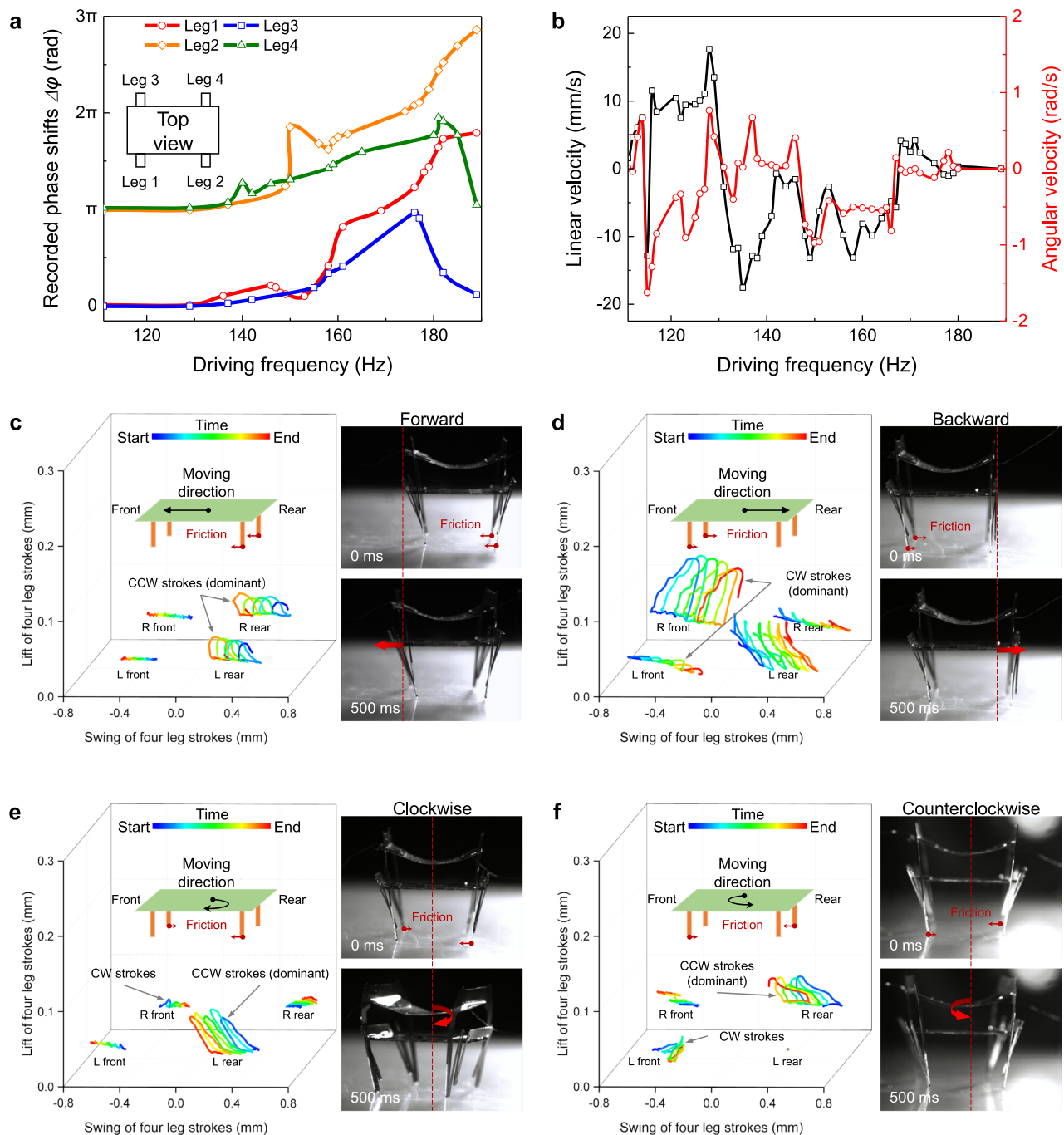


Fig. 2 | Steering mechanism of the robot. **a** The relationships between phase shifts and the driving frequency for the four individual legs. Even at the same frequency, the difference in each leg's phase shift results in the strokes of the four legs exhibiting different shapes, orientations, and inclinations, collectively contributing to various gaits of the robot. **b** The experimental linear velocity (mm/s) and angular

velocity (rad/s) of the robot with respect to the driving frequency. Trajectories of legs across multiple driving cycles in the locomotion of **(c)** forward (95 Hz), **(d)** backward (61 Hz), **(e)** CW (102 Hz) and **(f)** CCW (68 Hz) steering, respectively. Time begins at the blue end and flows to the red end. The friction forces from the ground are indicated by red arrows.

vibration modes is essential for the method of modal analysis in our soft robot. The corresponding design strategy is detailed in Supplementary Fig. 19–21 and Method 1.

Steering mechanism

The combinations of tunable strokes of four individual legs with various shapes (lines, circles, or ellipses), orientations (CW or CCW), and inclinations (positive or negative) can lead to various gaits to steer along a diverse range of paths. Although the robot is symmetrically designed, fabrication and assembly processes always result in slight

variations in four legs. As shown in Supplementary Fig. 22, the dynamic response of the suspended four legs (driven with 300 Volts) reveals two resonant peaks at 60 Hz and 138 Hz. The experiments show that resonance of all four legs occurs at the same frequency, albeit with slight variations in amplitudes, confirming minor distinctions among the four legs. Fig. 2a shows the relationships between phase shifts and driving frequencies for the four individual legs. Even at the same frequency, the difference in each leg's phase shift results in the strokes of the four legs exhibiting different shapes, orientations, and inclinations, collectively contributing to various gaits of the robot. Fig. 2b shows the

experimental linear velocity (mm/s) and angular velocity (rad/s) of the robot with respect to the driving frequency (driven with 300 Volts). Given these empirical data, the robot's movement can be controlled by selecting its driving frequency.

The ground-contact movement of a tethered prototype robot is recorded using two synchronous high-speed cameras arranged at two sides to capture the trajectories of the four legs. Fig. 2c–f show trajectories of legs across multiple driving cycles, with time progressing from blue to red. The trajectories demonstrate forward (95 Hz), backward (61 Hz), CW (102 Hz), and CCW (68 Hz) steering, respectively. Despite being driven at the same frequency, experiments indicate that legs exhibit distinct trajectories where the horizontal axis represents longitudinal swing of leg strokes and the vertical axis denotes vertical lift. A larger displacement indicates higher foot velocities, resulting in more forceful impacts with the ground. The direction and magnitude of the ground reaction force on each leg depend on the shapes, orientations, and inclinations of leg strokes. The frictional forces during CW and CCW strokes are directionally opposed (Supplementary Fig. 23). Thus, various combinations of ground reaction forces on four legs enable the robot to steer along a range of curvatures, including forward, backward, and diagonal directions.

For instance, as shown in Fig. 2c, the larger forward-directed ground reaction forces generated by the robot's two rear legs with CCW strokes result in the forward movement to the left, similar to a rear-drive mode. These strokes contrast with the configurations in Fig. 2d, where all four legs exhibit CW curves, leading to a backward movement to the right. The robot's steering is driven by a gait in which one leg provides the dominant thrust while the other three legs primarily slide. The friction forces from the ground, indicated by red arrows, play a key role in generating steering torques. In Fig. 2e, the robot exhibits CW steering when the left rear leg (with the greatest stroke amplitude) performs CCW strokes, while the right front leg performs CW strokes and the remaining two legs slide. The resulting CW torque, generated by friction forces, drives the robot's CW rotation. Similarly, in Fig. 2f, the robot exhibits CCW steering when the right rear leg (with the greatest stroke amplitude) executes CCW strokes, while the left front leg executes CW strokes, with minimal displacement of the left rear leg. The friction forces generate a CCW torque, leading to the robot's CCW rotation. These movements are further detailed in the slow-motion footage (Supplementary Movie 5).

Flexible and resilient exoskeleton

The exoskeletons of cockroaches exhibit a remarkable ability to endure structural deformation, allowing them to thrive in various harsh environments³⁴. Inspired by origami structures, our robot's exoskeleton is designed with compliant linkages, enabling it to withstand significant deformations. Experiments show that the robot can endure extreme loads: 125% longitudinal stretching, 50% vertical compression, and 20° twisting. As shown in Fig. 3a, the experimental results (1st row) closely match the finite element method (FEM) simulations (2nd row) conducted in Abaqus software. Slow-motion footage in Supplementary Movie 6 illustrates the exoskeleton's recovery capability, highlighting its flexibility and robustness. The exoskeleton's serpentine structures function like torsion springs, allowing large deformation and rapid recovery, which are critical for survival in demanding conditions.

The use of soft materials enhances the exoskeleton's resilience by eliminating fragile components such as circuits and power supplies, which are prone to breakage. For practical applications, an entire untethered microsystem must be robust enough to negotiate complex environments³⁵. The robustness is demonstrated in an experiment involving a 1.12 g and 2 cm robot equipped with onboard circuits and batteries, which is subjected to compression under a ruler, as shown in Fig. 3b. The robot's compressibility, defined as the ratio of the robot's height change with respect to its original height, is captured in the

slow-motion footage in Supplementary Movie 6. The origami-inspired exoskeleton allows the robot to sprawl and recover rapidly, compressing its central frame against the ground. The maximum compressibility is limited by the non-compressible nature of circuits and batteries. The high-speed video analysis shows that the untethered robot quickly returns to its original form, realigning its structure within 0.14 sec after the compressive force is removed. Fig. 3c presents the simplified schematics of foldable exoskeletons in both standing (left) and sprawled posture (right). The exoskeletons facilitate the sprawling with legs folding oppositely under a considerable large load, effectively protecting fragile components. Despite the non-compressible battery and circuit board, the robot achieves a high compression ratio of 66%, similar to that of cockroaches³⁴. The untethered robot's robustness is further demonstrated by withstanding the weight of an adult human (63.7 kg), as shown in Fig. 3d–f. Remarkably, the robot's locomotion performance remains almost unaffected even after bearing the load over 53,000 times its weight (Supplementary Move 6). This is the first untethered robot of its scale (~1 g) to be functioning continuously after being stepped on. To evaluate its practicality in varied environments, free-fall tests are conducted (Fig. 3g–i and Supplementary Movie 7). The untethered robot, running and dropping from an 8 cm high stage, lands safely due to its flexible and resilient exoskeletons. Over 44 trials, the landing outcomes are 40% upright, 30% upside-down, and 30% for the other two postures. The robot can retain controllability post-landing with upright and upside-down postures (Supplementary Movie 7) to achieve a total success rate of 70%, enhancing its adaptability and preventing catastrophic falls in uneven terrains. As shown in Supplementary Fig. 24 and Movie 8, the robot is capable of traversing sideways across rough terrain consisting of sand mixed with small gravel, illustrating its adaptability to irregular surfaces. However, its running speed is significantly reduced to 0.2 BL/s compared to its performance on flat ground. The robot's slope climbing capability is demonstrated in Supplementary Fig. 25 and Movie 8. It achieves a speed of 2.3 BL/s on a 7° incline and 1.9 BL/s on a 10° incline.

Untethered configurations and state-of-the-art comparison

The design of our microrobot allows for seamless transition from a tethered to an untethered configuration by adding components to its central suspension (carbon-fiber frame) without altering its fundamental structure. The serpentine exoskeletons utilize elastic suspension to protect the loading area from interference caused by the bending actuator and ground substrate. Consequently, a certain payload does not significantly impact the actuator's performance, ensuring that the robot's mobility remains stable when transitioning from tethered to untethered form. As shown in Fig. 4a, the untethered microrobot consists of a base prototype (260 mg, including a 30 mg unimorph and 230 mg exoskeletons), a rechargeable lithium battery (375 mg; 4.2 V, 12 mAh, GMB Power Inc.), and a circuit board (485 mg), totaling 1.12 g. Generating several hundreds of volts in lightweight electronics for piezoelectric actuators has proven challenging³⁶. The energy efficiencies of each stage of the conversion from battery to leg thrust are discussed in Supplementary Method 2 and Fig. 26–33^{36–39}. The circuit board measuring 1 cm × 1 cm in size and 485 mg in weight can generate around 500-Vpp square waves within a frequency range of 1 Hz to 1.75 kHz to power the actuator (details in Supplementary Fig. 27 and Table 3). Locomotion commands are wirelessly transmitted via a cell-phone using a Bluetooth low-power chip NRF52832 (by Nordic Semiconductor). The total Cost of Transport (CoT) for the untethered robot is 117, estimated as $\text{CoT} = \text{UI/mgv} = 4.2 \text{ V} \times 0.03 \text{ A} / (1.12 \times 10^{-3} \text{ kg} \times 10 \text{ m/s}^2 \times 0.096 \text{ m/s})$. Fully charged, the robot can travel 30 meters in 8 min at an average speed of 60 mm/s (3 BL/s). Potential strategies for optimizing power consumption are discussed in Supplementary Method 2.

Autonomous movement with integrated power and control systems is crucial for achieving long-range autonomy in microrobots¹.

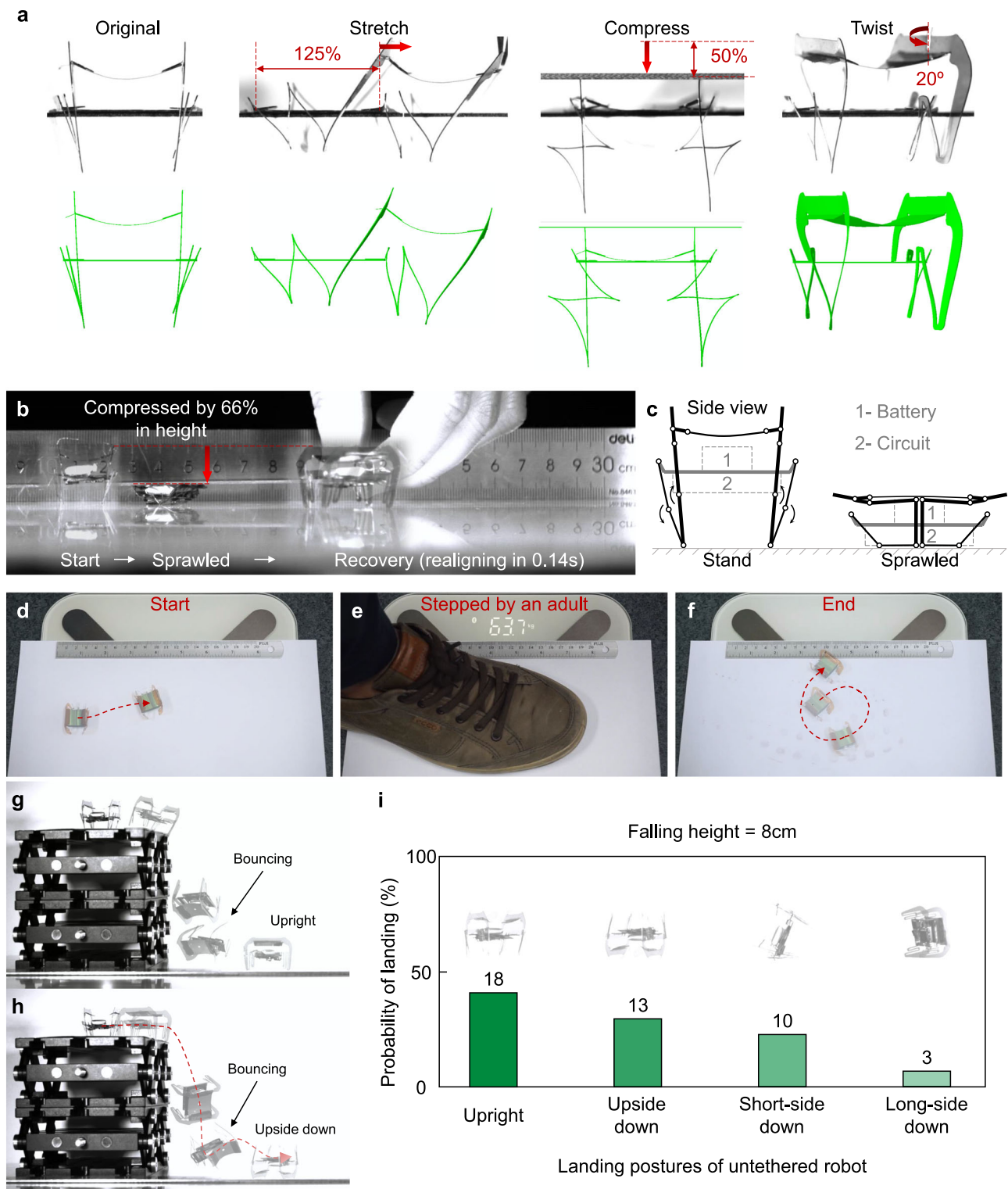


Fig. 3 | Robust performance. **a** Experimental results and FEM simulations of a base robot that is tested with stretching, compression, and twisting, respectively. **b** An untethered robot becomes sprawled by laying a ruler onto the back of the robot. **c** Simplified schematics of the foldable exoskeleton in the unconfined standing (left) and confined sprawled postures (right), respectively. **d–f** The speed of an

untethered robot barely declines after being stomped on by a 63.7-kg-weight adult human. The landed untethered robot demonstrates maneuverability in both **(g)** upright and **(h)** upside down postures. **i** Statistics of four landing postures of the untethered robot.

Speed, a key performance metric, is compared in Fig. 4b, which shows relative speeds of published untethered microrobots weighing less than 3g^{28–30,32,40–46}, including rigid robots (triangles), soft robots (circles), and this soft robot (red star). As shown the red dash mark line in Fig. 4b, our robot exhibits the highest relative speed (4.8 BL/s) in its

untethered class weighing less than 1.5 g. Fig 4c explores the relationship between maneuverability of microrobots (<3 g)^{11,14,15,17,18,28,30,32,42,43,45–47} and the number of actuators employed. Maneuverability is a comprehensive metric which combines running and turning performance⁴⁸. Here, relative forward speed (BL/s) ×

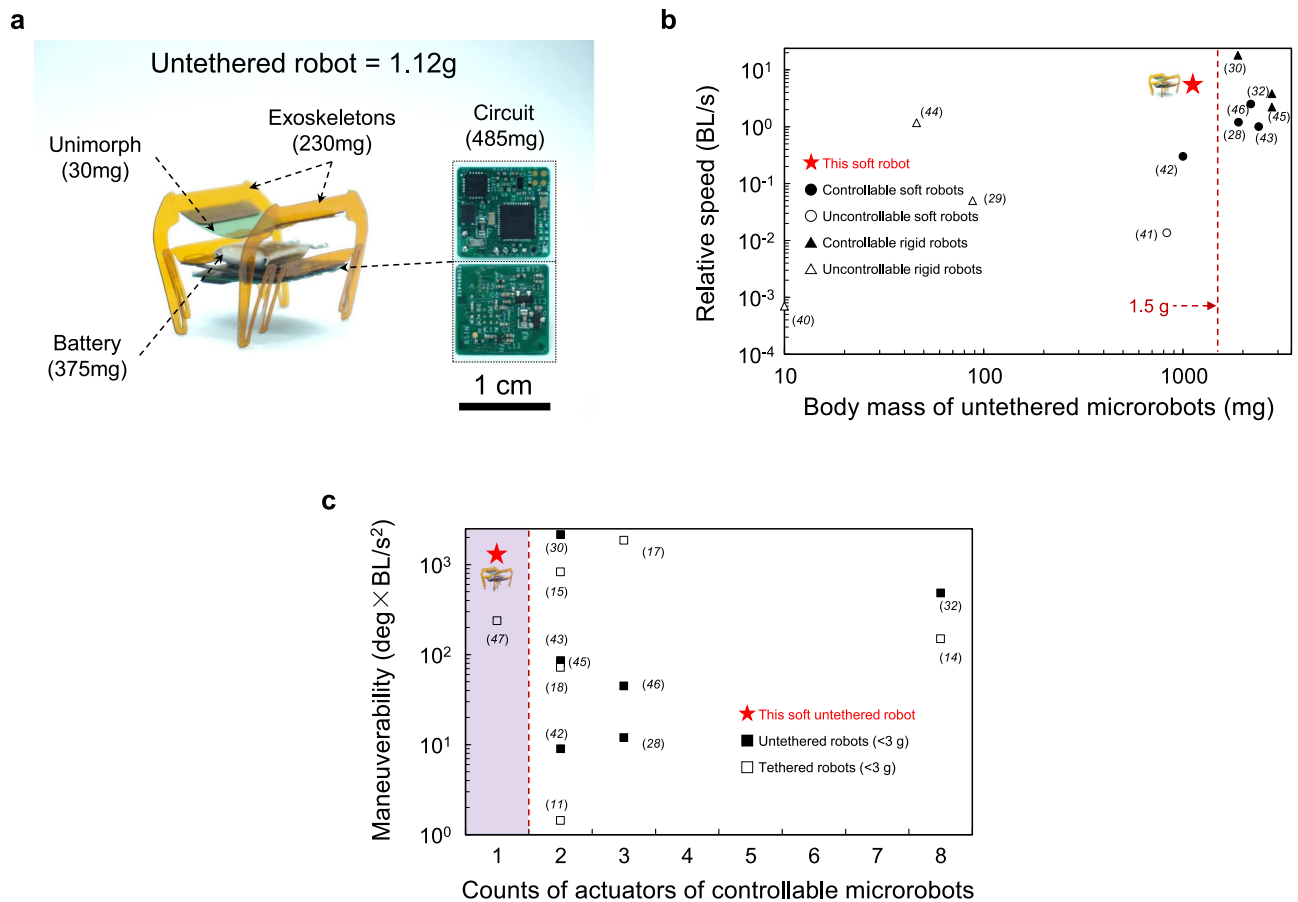


Fig. 4 | Untethered configurations and comparison of state-of-the-art untethered microrobots (mass < 3 g). **a** An untethered microrobot with the weight of 1.12 g consists of a single unimorph, compliant exoskeletons, control circuits, and a rechargeable battery. **b** Relative speed of untethered microrobots plotted against their body masses. The data indicated by hollow are uncontrollable while those indicated by solid are controllable. The circles indicate soft robots and triangles indicate rigid robots, respectively. The dashed vertical line marks a body mass of

1.5 g. **c** Maneuverability vs. counts of actuators of controllable microrobots (<3 g). The maneuverability is calculated as relative forward speed (BL/s) \times angular turning speed (deg/s). Our single-actuated robot (red star) uniquely achieves an outstanding maneuverability while other untethered microrobots usually need two or more actuators to obtain comparable performance. The solid squares indicate untethered microrobots while the hollow ones are tethered. For data, see Supplementary Table 4.

angular turning speed (deg/s) are used to evaluate maneuverability ($\text{deg} \times \text{BL/s}^2$) of microrobots.

Among untethered microrobots weighing less than 3 g, our single-actuated robot (red star) uniquely achieves an outstanding maneuverability while other microrobots usually need two or more actuators to obtain comparable performance (data in Supplementary Table 4). Our earlier work also utilizes frequency-dependent control to manipulate the robot⁴⁷. The directional control of the earlier robot was achieved through an asymmetric design, where biased holes created an unbalanced mass distribution. This asymmetry served as the turning strategy by inducing uneven vibration amplitudes among four legs. Due to the lack of tunable stroke patterns—such as transitions between CW and CCW strokes—our earlier robot was unable to perform a wide range of steering maneuvers, including reverse motion and reverse steering. In contrast, the current robot employs a new design principle based on serpentine structures. Each leg can generate diverse trajectory patterns—such as lines, ellipses, and circles—with controllable orientations (CW and CCW) and inclinations (positive and negative). This design enables a more versatile and reconfigurable locomotion strategy, which provides forward motion, turning while moving forward, reverse motion, and turning while reversing. The comparison in Fig. 4c highlights the high efficiency of our novel turning strategy with solo actuating. Additionally, according to the scaling effect, further miniaturization of this robot could lead to higher maneuverability.

Comprehensive demonstrations

Our design features an untethered robot weighing 1.12 g and measuring 2 cm, with impressive locomotion capabilities. As illustrated in Fig. 5a, the robot, equipped with control circuits and a rechargeable battery, navigates a designed path (following the driving frequencies of 179 Hz, 164 Hz, 172 Hz, and 177 Hz) at a maximum relative speed of 4.8 BL/s (9.6 cm/s). Fig. 5b and c showcase the CW (driven at 184 Hz) and CCW (driven at 162 Hz) angular velocities of 4.88 rad/s (280 °/s) and 3.14 rad/s (180 °/s), respectively. Remarkably, the microrobot can perform a drifting maneuver by planting one leg, achieving a minimum turning radius of 1 cm—only half its body length. These movements are documented in Supplementary Movie 9. The ability to navigate tight turns, a challenge for many untethered microrobots, significantly enhances its potential for operation in confined spaces. To enable closed-loop trajectory control, a custom infrared (IR) sensor module has been integrated into our untethered robot. Two IR sensors enable binary detection of the robot's position relative to a tracking line. The integrated untethered robot system—including the base robot, battery, control circuit, and IR sensor module—weighs 1.7 g. As shown in Supplementary Fig. 34 and Movie 10, the untethered robot successfully follows a dark navigation line with an average tracking speed of 0.3 cm/s. The robot dynamically adjusts its trajectory in response to sensor feedback, and achieves autonomous path correction with only a single actuator. Detailed implementation procedures are provided in Supplementary Method 3.

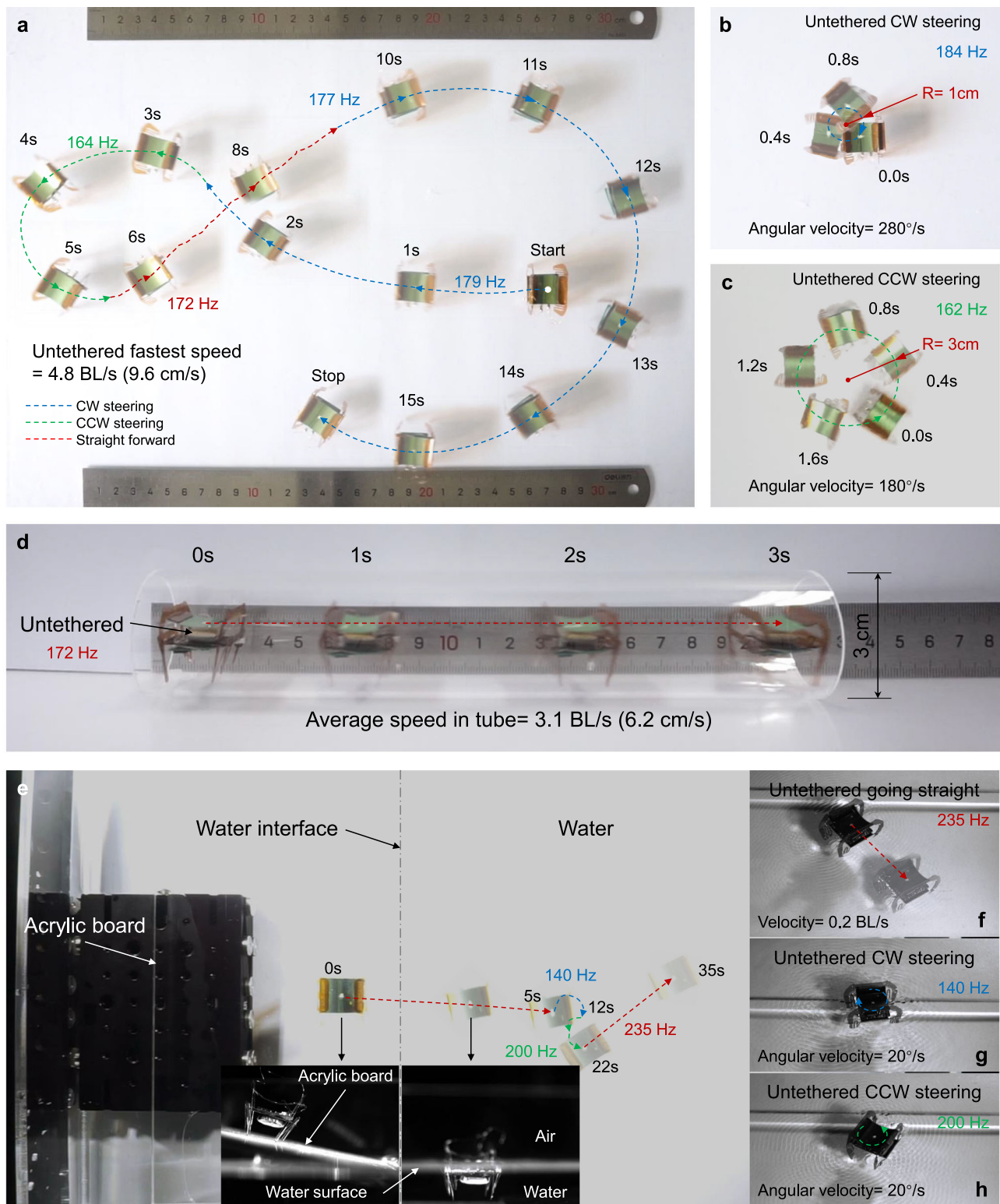


Fig. 5 | Comprehensive demonstrations. The untethered microrobot demonstrates the locomotion of: (a) designed path, (b) CW and (c) CCW steering. The maximum relative speed and angular velocity is 4.8 BL/s (9.6 cm/s) and 4.88 rad/s ($280^\circ/\text{s}$), respectively. **d** The untethered microrobot travels through a narrow quartz tube with an average relative speed of 3.1 BL/s (6.2 cm/s). **e** An untethered

microrobot transits from an acrylic board to the water surface. The two insets show the side views on an inclined acrylic board and the water surface, respectively. **f–h** the locomotion of the microrobot with straight, CW and CCW motions on the water's surface, respectively.

To further validate its performance in narrow environments, the untethered robot driven at 172 Hz is tested inside a transparent quartz tube with an inner diameter of 3 cm, as shown in Fig. 5d. As recorded in Supplementary Movie 11, the robot maintains an average relative speed

of 3.1 BL/s (6.2 cm/s). Additionally, the robot can traverse water's surface. Fig. 5e and Supplementary Movie 11 demonstrate the robot's smooth transition from land to water, descending from an inclined acrylic board onto the surface of deionized water. The insets of Fig. 5e

provide side views of the robot on both an acrylic board and the water's surface. The robot's upper body remains above the water while its lower body is submerged, supported by surface tension due to its low mass and compact size. When skating on the water's surface, the robot's four legs act as paddles to generate thrust. Similar to its land locomotion, the robot exhibits controllable steering on water. Fig 5f–h show forward (driven at 235 Hz) speed on water at 0.2 BL/s, with both CW (driven at 140 Hz) and CCW (driven at 200 Hz) steering speeds recorded at 20 °/s.

Discussion

This research represents an advancement in the development of autonomous, agile, and robust microrobots with controllable locomotion using a single actuator in both upright and upside-down postures. Unlike conventional microrobots typically using two or more actuators for tunable leg strokes, the steering by a single actuator reduces the weight, size, control complexity, and energy consumption by converting the bending movement of a unimorph to tunable leg strokes with various shapes, orientations, and inclinations. The combinations of various leg stroke patterns operated in high frequencies can result in an outstanding maneuverability for a soft untethered robot weighing 1.12 g and measuring 2 cm in length. The extraordinary resilience due to its flexible, origami-based exoskeletons enables the first untethered microrobot to survive being stepped on and to maintain controllability. Furthermore, it showcases adaptability by closed-loop trajectory control, navigating through narrow tubes, and moving on the water's surface. Future directions and challenges would include (i) integrating additional locomotion modes such as jumping, gliding, or flying to enhance adaptability in unstructured environments; (ii) implementing algorithms among large groups of microrobots for swarm manipulation; (iii) improving energy harvesting and storage technologies to extend the lifespan of microrobots. Further investigation and optimization are essential to unlock practical applications that demand an underactuated microsystem, where minimalism and high efficiency are crucial.

Methods

The base prototype robot consists of a single PET/PVDF unimorph actuator, two compliant polyimide exoskeletons, and a carbon-fiber frame. Detailed fabrication and assembly methodologies are depicted in Supplementary Fig. 1. The PET/PVDF unimorph actuator is constructed with a 50- μ m-thick PET tape (sourced from Gizmo Dorks) as the top substrate, and a 20- μ m-thick PVDF film (supplied by PolyK Technologies, LLC) as the bottom artificial muscle. The PVDF film is patterned with ultra-thin electrodes, consisting of 5-nm-thick chromium and 50-nm-thick gold layers on each side. Both the PVDF film and PET tape are precision-cut using a paper-cutting machine (manufactured by Silhouette America), and then laminated to form a rectangular-shaped unimorph, as illustrated in Supplementary Fig. 1a. Connectivity is established via two copper wires, each one mil in diameter, which are affixed to the electrode sides of the PVDF film using a conductive tape. The exoskeletons, crafted from 120- μ m-thick PI film, are also cut using the paper-cutting machine, with specific regions intricately incised to create crevices that facilitate folding during the assembly process (Supplementary Fig. 1b). A 200- μ m-thick carbon-fiber frame is shaped with hollowed sections through laser machining (Supplementary Fig. 1c). The final assembly process involves the integration of the unimorph, exoskeleton, and carbon-fiber frame, which are securely held together using double-sided adhesive tapes, as depicted in Supplementary Fig. 1d.

Data availability

All data that support the findings of this study are available within the article and its Supplementary Information and from the corresponding author Yichuan Wu upon request.

References

- Pierre, R. S. & Bergbreiter, S. Toward autonomy in sub-gram terrestrial robots. *Annu. Rev. Control Robot. Auton. Syst.* **2**, 231–252 (2019).
- Yang, G. Z. et al. The grand challenges of science robotics. *Sci. Robot.* **3**, eaar7650 (2018).
- Rich, S. I., Wood, R. J. & Majidi, C. Untethered soft robotics. *Nat. Electron.* **1**, 102–112 (2018).
- Yasuda, T., Shimoyama, I. & Miura, H. Microrobot actuated by a vibration energy field. *Sens. Actuators A: Phys.* **43**, 366–370 (1994).
- Matsuoka, T. et al. Mechanical analysis for micro mobile machine with piezoelectric element. In *Proc. IEEE/RSJ Int. Conf. Intell. Robots Syst.*, 1685–1690 (1993).
- Yan, Y., Shui, L., Liu, S., Liu, Z. & Liu, Y. Terrain adaptability and optimum contact stiffness of vibro-bot with arrayed soft legs. *Soft Robot.* **9**, 981–990 (2022).
- loi, K. et al. A mobile micro-robot using centrifugal forces. In *Proc. IEEE/ASME Int. Conf. Adv. Intell. Mechatron.*, 736–741 (1999).
- Ju, J., Wang, Q. & Zhang, K. Design and analysis of a novel micro-robot driving platform. In *Proc. Inst. Mech. Eng. C*. **233**, 3849–3857 (2019).
- Wu, Y. et al. Insect-scale fast moving and ultrarobust soft robot. *Sci. Robot.* **4**, eaax1594 (2019).
- Gu, G., Zou, J., Zhao, R., Zhao, X. & Zhu, X. Soft wall-climbing robots. *Sci. Robot.* **3**, eaat2874 (2018).
- Lee, D., Kim, S., Park, Y.-L. & Wood, R. J. Design of centimeter-scale inchworm robots with bidirectional claws. In *Proc. IEEE Int. Conf. Robot. Autom.*, 3197–3204 (2011).
- Saito, K. et al. Miniaturized rotary actuators using shape memory alloy for insect-type MEMS microrobot. *Micromachines* **7**, 58 (2016).
- Contreras, D. S. & Pister, K. S. J. First steps of a millimeter-scale walking silicon robot. In *Proc. IEEE Int. Conf. Solid-State Sens. Actuators Microsyst.*, 910–913 (2017).
- Goldberg, B., Doshi, N. & Wood, R. J. High speed trajectory control using an experimental maneuverability model for an insect-scale legged robot. In *Proc. IEEE Int. Conf. Robot. Autom.*, 3538–3545 (2017).
- Chen, R. et al. Legless soft robots capable of rapid, continuous, and steered jumping. *Nat. Commun.* **12**, 7028 (2021).
- Wang, D. et al. Dexterous electrical-driven soft robots with reconfigurable chiral-lattice foot design. *Nat. Commun.* **14**, 5067 (2023).
- Wang, W., Deng, J., Li, J., Zhang, S. & Liu, Y. A small and agile ring-shaped tripodal piezoelectric robot driven by standing and traveling mechanical waves. *IEEE Trans. Ind. Electron.* **71**, 2769–2778 (2024).
- Kim, S., Johnson, A. M. & Bergbreiter, S. Picotaur: A 15 mg hexapodal robot with electrostatically driven, 3D-printed legs. *Adv. Intell. Syst.* **6**, 2400196 (2024).
- Park, S. J. et al. Phototactic guidance of a tissue-engineered soft-robotic ray. *Science* **353**, 158–162 (2016).
- Zhu, H. et al. Self-powered locomotion of a hydrogel water strider. *Sci. Robot.* **6**, eaabe7925 (2021).
- Miskin, M. Z. et al. Electronically integrated, mass-manufactured, microscopic robots. *Nature* **584**, 557–561 (2020).
- Shin, B. et al. Hygrobot: A self-locomotive ratcheted actuator powered by environmental humidity. *Sci. Robot.* **3**, eaar2629 (2018).
- Luo, D. et al. Autonomous self-burying seed carriers for aerial seeding. *Nature* **614**, 463–470 (2023).
- Hu, W., Lum, G. Z., Mastrangeli, M. & Sitti, M. Small-scale soft-bodied robot with multimodal locomotion. *Nature* **554**, 81–85 (2018).
- Kim, K., Yuk, H., Zhao, R., Chester, S. A. & Zhao, X. Printing ferromagnetic domains for untethered fast-transforming soft materials. *Nature* **558**, 274–279 (2018).
- Miyashita, S., Guitron, S., Li, S. & Rus, D. Robotic metamorphosis by origami exoskeletons. *Sci. Robot.* **2**, eaao4369 (2017).
- Mao, G. et al. Ultrafast small-scale soft electromagnetic robots. *Nat. Commun.* **13**, 4456 (2022).

28. Liang, J. et al. Electrostatic footpads enable agile insect-scale soft robots with trajectory control. *Sci. Robot.* **6**, eabe7906 (2021).
29. Yang, X., Chang, L. & Pérez-Arancibia, N. O. An 88-milligram insect-scale autonomous crawling robot driven by a catalytic artificial muscle. *Sci. Robot.* **5**, eaba0015 (2020).
30. Yu, X. et al. Forward and backward control of an ultrafast millimeter-scale microrobot via vibration mode transition. *Sci. Adv.* **10**, eadr1607 (2024).
31. Zarrouk, D. & Fearing, R. S. Controlled in-plane locomotion of a hexapod using a single actuator. *IEEE Trans. Robot.* **31**, 157–167 (2015).
32. Goldberg, B. et al. Power and control autonomy for high-speed locomotion with an insect-scale legged robot. *IEEE Robot. Autom. Lett.* **3**, 987–993 (2018).
33. Chen, Y., Doshi, N., Goldberg, B., Wang, H. & Wood, R. J. Controllable water surface to underwater transition through electro-wetting in a hybrid terrestrial-aquatic microrobot. *Nat. Commun.* **9**, 2495 (2018).
34. Jayarama, K. & Full, R. J. Cockroaches traverse crevices, crawl rapidly in confined spaces, and inspire a soft, legged robot. In *Proc. Natl. Acad. Sci. USA* **113**, E950–E957 (2016).
35. Chong, B. et al. Multilegged matter transport: a framework for locomotion on noisy landscapes. *Science* **380**, 509–515 (2023).
36. Steltz, E., Seeman, M., Avadhanula, S. & Fearing, R. S. Power electronics design choice for piezoelectric microrobots. In *Proc. IEEE/RSJ Int. Conf. Intell. Robots Syst.*, 1322–1328 (2006).
37. Fearing, R. S. et al. Wing transmission for a micromechanical flying insect. In *Proc. IEEE Int. Conf. Robot. Autom.*, 1509–1516 (2000).
38. Steltz, E. & Fearing, R. S. Dynamometer power output measurements of miniature piezoelectric actuators. *IEEE/ASME Trans. Mechatron.* **14**, 1–10 (2009).
39. Campolo, D., Sitti, M. & Fearing, R. S. Efficient charge recovery method for driving piezoelectric actuators with quasi-square waves. *IEEE Trans. Ultrason. Ferroelectr. Freq. Control.* **50**, 237–244 (2003).
40. Hollar, S., Flynn, A., Bellew, C. & Pister, K. Solar powered 10 mg silicon robot. In *Proc. IEEE Int. Conf. Micro Electro Mech. Syst.*, 706–711 (2003).
41. Must, I. et al. Ionic and capacitive artificial muscle for biomimetic soft robotics. *Adv. Eng. Mater.* **17**, 84–94 (2015).
42. Ji, X. et al. An autonomous untethered fast soft robotic insect driven by low-voltage dielectric elastomer actuators. *Sci. Robot.* **4**, eaaz6451 (2019).
43. Hoover, A. M., Steltz, E. & Fearing, R. S. RoACH: an autonomous 2.4 g crawling hexapod robot. In *Proc. IEEE/RSJ Int. Conf. Intell. Robots Syst.*, 26–33 (2008).
44. Zhu, Y. et al. A 5-mm untethered crawling robot via self-excited electrostatic vibration. *IEEE Trans. Robot.* **38**, 719–730 (2021).
45. Iyer, V., Najafi, A., James, J., Fuller, S. & Gollakota, S. Wireless steerable vision for live insects and insect-scale robots. *Sci. Robot.* **5**, eabb0839 (2020).
46. Miao, Z. et al. Power autonomy and agility control of an untethered insect-scale soft robot. *Soft Robot.* **10**, 749–759 (2023).
47. Liang, J. et al. Manipulating the moving trajectory of insect-scale piezoelectric soft robots by frequency. In *Proc. IEEE Int. Conf. Micro Electro Mech. Syst.*, 1041–1044 (2019).
48. Zarrouk, D., Haldane, D. & Fearing, R. S. Dynamic legged locomotion for palm-size robots. In *Proc. SPIE Int. Soc. Opt. Eng.*, 9467 (2015).

Acknowledgements

This work is supported by National Natural Science Foundation of China (grant 52005083, Y. W.) and Sichuan Provincial Department of Science and Technology (grant 2024NSFSC0144, Y. W.).

Author contributions

Y.W. conceived the prototype, analyzed the results, wrote the paper, and supervised the research. L.C., G.L., and P. W. performed the experiments and developed the circuits. L. R. and B. P. assisted with the modal analysis.

Competing interests

The authors declare no competing interests.

Additional information

Supplementary information The online version contains supplementary material available at <https://doi.org/10.1038/s41467-025-61810-1>.

Correspondence and requests for materials should be addressed to Yichuan Wu.

Peer review information *Nature Communications* thanks Xiaojun Yan, who co-reviewed with Wencheng Zhan, and the other, anonymous, reviewer(s) for their contribution to the peer review of this work. A peer review file is available.

Reprints and permissions information is available at <http://www.nature.com/reprints>

Publisher's note Springer Nature remains neutral with regard to jurisdictional claims in published maps and institutional affiliations.

Open Access This article is licensed under a Creative Commons Attribution-NonCommercial-NoDerivatives 4.0 International License, which permits any non-commercial use, sharing, distribution and reproduction in any medium or format, as long as you give appropriate credit to the original author(s) and the source, provide a link to the Creative Commons licence, and indicate if you modified the licensed material. You do not have permission under this licence to share adapted material derived from this article or parts of it. The images or other third party material in this article are included in the article's Creative Commons licence, unless indicated otherwise in a credit line to the material. If material is not included in the article's Creative Commons licence and your intended use is not permitted by statutory regulation or exceeds the permitted use, you will need to obtain permission directly from the copyright holder. To view a copy of this licence, visit <http://creativecommons.org/licenses/by-nc-nd/4.0/>.

© The Author(s) 2025